THE ASTROPHYSICAL JOURNAL, 389:739–755, 1992 April 20

HIGH-ENERGY GAMMA-RAY EMISSION FROM PION DECAY IN A SOLAR FLARE MAGNETIC LOOP

NATALIE MANDZHAVIDZE
Institute of Geophysics, Georgian Academy of Science, Tbilisi, 380093, Georgia, USSR
AND
REUVEN RAMATY
Laboratory for High Energy Astrophysics, Goddard Space Flight Center, Greenbelt, MD 29771
Received 1991 June 24; accepted 1991 October 23

ABSTRACT

We have investigated the production of high-energy gamma rays resulting from pion decay in a solar flare magnetic loop. We took into account magnetic mirroring, MHD pitch-angle scattering, and all of the relevant loss processes and photon production mechanisms. We treated the transport of both the primary ions and the secondary positrons resulting from the decay of the positive pions, as well as the transport of the produced gamma-ray emission. We calculated the distributions of the gamma rays as a function of atmospheric depth, time, emission angle, and photon energy and studied the dependence of these distributions on the model parameters. The obtained angular distributions are not sufficiently anisotropic to account for the observed limb brightening of the greater than 10 MeV flare emission, indicating that the bulk of this emission is bremsstrahlung from primary electrons. We compared our calculations with the available data for pion decay radiation from the 1982 June 3 flare and considered the possible models of particle transport and gamma-ray production for this flare.

Subject headings: MHD — Sun: flares — Sun: particle emission — Sun: X-rays, gamma rays

1. INTRODUCTION

The observations of gamma rays and neutrons from solar flares and their interpretations have been reviewed in several publications (Chupp 1984; Ramaty & Murphy 1987; Rieger 1989; Chupp 1990). In the present paper we deal with high-energy (>10 MeV) gamma rays resulting from the decay of neutral and charged pions in solar flares. Gamma-ray emission at energies greater than 10 MeV, resulting predominantly from the bremsstrahlung of primary electrons, was observed (Rieger 1989) from more than 20 flares with the gamma-ray spectrometer flown on the *Solar Maximum Mission* (*SMM*/GRS). Pion emission was first observed from the 1982 June 3 flare (Forrest et al. 1985, 1986; Forrest 1988), where the pionic component was clearly separated from both the bremsstrahlung of the primary electrons and the neutrons which were also detected with the *SMM*/GRS (Chupp et al. 1987). In addition, there is marginal evidence for pionic emission from several other flares, most notably the 1984 April 24 flare. Pions in solar flares are produced predominantly by protons and α-particles in the energy range from a few hundred MeV/nucleon to a few GeV/nucleon interacting with the ambient solar atmosphere. The neutral pions decay into gamma rays directly. The charged pions produce gamma rays by decaying (via muons) into secondary electrons and positrons, which produce photons via bremsstrahlung and annihilation in flight. These processes were treated in detail by Murphy, Dermer, & Ramaty (1987).

The transport of ions and relativistic electrons in magnetized solar flare loops, and the related problem of gamma-ray production, have received considerable attention (see Ramaty et al. 1990). The transport of ions, including the application of the mirror force in a convergent magnetic flux tube, was first treated by Zweibel & Haber (1983), who emphasized the effects of the trapping of the particles and their precipitation due to MHD pitch-angle scattering on the time dependence of the nuclear de-excitation line emission. The effects of magnetic mirroring in convergent magnetic flux tubes on the angular distribution of greater than 10 MeV primary electron bremsstrahlung was first considered by Semukhin & Kovaltsov (1985), who showed that the limb brightening (Rieger et al. 1983; Rieger 1989) of the greater than 10 MeV emission could be explained by such mirroring (see also Petrosian 1985; Dermer & Ramaty 1986; Kocharov et al. 1987; Miller & Ramaty 1989; MacKinnon & Brown 1989, 1990; Kocharov & Kovaltsov 1990). The problem of greater than 10 MeV bremsstrahlung production in flares on the solar disk was addressed by Ramaty et al. (1988), who pointed out that in such flares the ultrarelativistic electrons must be producing gamma rays as they move up in the solar atmosphere and that this is most likely to happen after multiple bounces between the mirror points. Monte Carlo codes for nuclear de-excitation line production and greater than 10 MeV bremsstrahlung production, taking into account magnetic mirroring and MHD pitch-angle scattering, were developed by Hua, Ramaty, & Lingenfelter (1989) and Miller & Ramaty (1989). These authors calculated gamma-ray time profiles for a broad range of turbulent energy densities and emphasized the case of saturated pitch scattering in which the particles are isotropized in the coronal portion of the loop on a time scale comparable to their transit time through the loop (see also Kennel & Petschek 1966; Kennel 1969). Hua et al. (1989) and Miller & Ramaty (1989) showed that the short durations of the decaying portions of the gamma-ray time profiles in impulsive flares could be understood in loop models with the pitch-angle scattering rate close to saturation.

The transport of high-energy ions and the production of neutrons and neutral pions in loop models were treated by Kocharov et al. (1987), without including the effects of MHD pitch-angle scattering, and by Gueglenko et al. (1990a, b), who

took scattering into account. These authors showed that the effects of the trapping of particles in magnetic loops would be most evident in the time profiles of pion decay emission, because of all the observed solar flare gamma-ray components, this emission is produced by ions of the highest energies and hence of the longest stopping ranges. Kocharov et al. (1988) and Gueglenko et al. (1990a, b) applied their calculations to the 1982 June 3 flare, suggesting that the two distinct pulses of the observed time profile of the pion radiation in this flare were the consequence of a variable precipitation rate of the trapped particles caused by variations in the energy density of the MHD turbulence. This interpretation of the 1982 June 3 observations differs from that of Murphy et al. (1987), who suggested that the second pulse of pion emission resulted from a second phase of particle acceleration in this flare.

In the present paper we carry out a detailed calculation of pion decay radiation in a solar flare loop, including the production of gamma rays from neutral pion decay, bremsstrahlung of secondary positrons and electrons, and annihilation in flight of the positrons. We show that the transport of the positrons can increase the anisotropy of the total pion emission. We also include the transport of photons in the solar atmosphere by taking into account the effects of Compton scattering and pair production. We evaluate the attenuation of the gamma rays, which turns out to be very significant, particularly in cases when the pitch-angle scattering rate is near saturation. We calculate the depth distributions of pion and gamma-ray production, the time and angular dependencies of the radiations, and the energy spectra of the escaping photons in various directions. We carry out our calculations for a broad range of mirror ratios and turbulent MHD energy densities. We also investigate the effects of variations in the assumed ambient gas density profile in the loop, the size of the loop, and the coronal magnetic field (which affects the trapped positrons).

We apply our results to the distribution on the Sun of the locations of flares observed at greater than 10 MeV, which is a measure of the angular radiation pattern of greater than 10 MeV flare emission. We show that the expected pion radiation pattern is not sufficiently anisotropic to account for the observed distribution. We also apply our calculations to the observed time profile and energy spectrum of pion radiation in the 1982 June 3 flare. In particular, we modify the one-phase acceleration model of Gueglenko et al. (1990a, b) to include MHD pitch-angle scattering in the first pulse. However, if the scattering rate during this pulse is high enough, essentially all of the accelerated particles are precipitated, requiring a second acceleration phase.

We describe the model and the physical processes in § 2, present numerical results in § 3, and compare our calculated distributions with observations in § 4. We summarize our results in § 5.

2. MODEL AND PHYSICAL PROCESSES

We consider a loop model consisting of a semicircular coronal portion of radius R joined to two radially aligned straight portions extending to the photosphere. We fix the transition between the coronal portion and the straight portions at 200 km above the photosphere. We assume that in the coronal portion the magnitude of the magnetic field B_c is constant and that below the transition (at $z = 0$) the field increases linearly with the depth, $B(z) = B_c(1 + z/h_B)$. We assume that the density n_c is constant in the coronal portion. Below the transition, that is, for the chromospheric and photospheric portions of the loop, we assume a simple atmospheric model characterized by an exponential density profile, $n(z) = n_{ph} \exp [(z - 2000)/h_a]$, where n_{ph} is the density of the photosphere. We fix $n_{ph} = 3.7 \times 10^{17}$ (Avrett 1981), but let h_a vary. This model is essentially the same as that used by Gueglenko et al. (1990b), but is not as detailed as the atmospheric models employed by Hua et al. (1989) and Miller & Ramaty (1989). Our simpler model, however, allows us to easily explore the effects of the atmospheric model by varying the density scale height h_a.

We release the accelerated ions isotropically at the top of the loop. Since the pions are produced mainly in nuclear reactions between protons and α-particles, we have considered only these species in our treatment. We take the He-to-H ratio in the ambient gas equal to 0.07. We assume that the protons and α-particles have the same initial spectrum as a function of energy per nucleon and that the α-particle–to–proton ratio at the same energy per nucleon is also 0.07. A variety of spectral shapes have been used in previous calculations of gamma-ray production in solar flares (Ramaty & Murphy 1987). These include the Bessel function appropriate for stochastic acceleration in the nonrelativistic region (Ramaty 1979) and the shock acceleration spectrum proposed by Ellison & Ramaty (1985). In the present paper, for simplicity, we have used a power-law spectrum in kinetic energy per nucleon with the same spectral index γ for both the protons and α-particles. We find that our results are not strongly dependent on the assumed spectrum of the accelerated ions.

Since our Monte Carlo technique is similar to that used by Gueglenko et al. (1990b), we only present a brief description of it here. We choose the initial particle energy E_0 and the energy at interaction E_{int} randomly. We assume that each particle produces a pion with an appropriate weight, which takes into account the initial spectrum of the accelerated particles and the probability of pion production during the slowing down from E_0 to E_{int}. The latter depends on the nuclear cross sections for pion production, the removal of the particles by nuclear collisions, and rates of energy loss due to Coulomb interactions in the ambient gas. We have used the stopping powers for an ionized gas in the coronal region and for a neutral gas below the transition. We have ignored the effects of elastic nuclear collisions on the primary particles. By comparing our calculations with those of Murphy et al. (1987), who included elastic scattering as a loss process but not as an additional particle source, we see that ignoring elastic scattering as a loss increases the pion production by about 30%. On the other hand, Murphy et al. (1987) showed that the contribution to the total pion production of the secondary protons resulting from both elastic and inelastic nuclear collisions is less than 50% for very flat primary proton spectra, and significantly less than this value for steeper spectra. Since these two effects (removal and addition) nearly cancel each other, we have neglected both effects. The neglect of elastic nuclear collisions can also be justified as follows: In proton-proton collisions, elastic scattering becomes important relative to Coulomb and inelastic interactions mainly in the energy region 500–1000 MeV, where the elastic differential cross section in the center of mass system is strongly peaked in the forward and backward directions. This means that one of the secondary protons will move with practically the same velocity and angle as the primary proton, while the other will essentially stop. Thus, essentially the effect of the elastic scattering is to replace one primary proton with

one secondary proton. Concerning proton-helium interactions, the inelastic cross section dominates the elastic cross section at all energies of interest.

Particle transport is governed by the mirror force in the chromospheric and photospheric regions and by pitch-angle scattering due to resonant interactions with Alfvén turbulence in the corona. Below the transition in scattering can be neglected because of the rapid damping of the turbulence there. We have modeled the process of pitch-angle diffusion by considering many discrete small-angle scatterings. The path λ traversed between two scatterings is the main modeling parameter and is related to the energy density of the turbulence. After each scattering we change the pitch-angle cosine μ by an amount $\Delta\mu = (\Delta\mu)_1 + (\Delta\mu)_2$, where $(\Delta\mu)_1$ is chosen from a Gaussian distribution with standard deviation $\langle\Delta\mu^2\rangle = 2D_{\mu\mu}\lambda/v$ and $(\Delta\mu)_2 = D_\mu\lambda/v$, where $D_\mu = \partial D_{\mu\mu}/\partial\mu$. $D_{\mu\mu}$ is the pitch-angle scattering coefficient, which in the quasi-linear approximation is given by $D_{\mu\mu} = \pi^2 W_0 v r_L^{q-2}\mu^{q-1}(1-\mu^2)/B_c^2$ (Jokipii 1966; Palmer & Jokipii 1981; see also Hua et al. 1989 and Miller & Ramaty 1989). Here, $W(k) = W_0 k^{-q}$ is the power spectrum of the turbulence, and v and r_L are the velocity and Larmor radius of the particle. We have assumed that $W(k)$ is given by a Kolmogorov spectrum, that is, that $q = 5/3$.

In our modeling we have taken

$$\langle\Delta\mu^2\rangle = \Delta_0^2\,\mu^{q-1}(1-\mu^2)\,, \tag{1}$$

where Δ_0 is a constant. In order to provide an accurate simulation of scattering, Δ_0 has to be sufficiently small. In our calculations we have taken $\Delta_0 = 0.08$ (see discussion in the appendix of Gueglenko et al. 1990b).

The step size λ between two scatterings depends on the rigidity of the particle. From equation (1) and the expression of $D_{\mu\mu}$ given above, it follows that λ is proportional to $(A/Zp)^{2-q}$, where A, Z, and p are atomic mass, charge, and momentum per nucleon of the particle. From the same two equations one can also deduce the relationship between λ and the total energy density in the turbulence,

$$W_{\rm tot} = \int_{k_{\rm min}}^{\infty} W_0 k^{-q}\,dk = \frac{\Delta_0^2}{2\lambda\pi^2(q-1)} B_c^2 r_L^{2-q} k_{\rm min}^{1-q}\,. \tag{2}$$

If we take $B_c = 100$ G and $k_{\rm min}$ equal to the resonant wave number corresponding to 10 GeV protons, then $W_{\rm tot} = 4.9 \times 10^5/\lambda(30\ {\rm MeV})$, where $\lambda(30\ {\rm MeV})$ is the scattering length for 30 MeV protons.

We follow each proton and α-particle until their energy decreases to the interaction energy, $E_{\rm int}$. Between each two scatterings, we calculate the elapsed time and multiply the weight by the corresponding survival probability. The motion between scatterings can include multiple penetrations below the transition. When the energy $E_{\rm int}$ is reached, we calculate the location of the interaction, the pitch angle of the interacting particle, and the total elapsed time.

Pions in solar flares are produced mainly in p–p, p–α, and α–p interactions. We have neglected pion production in α–α interaction, which we estimate to contribute no more than 2% to the total production. Cross sections of pion production in the p–p reaction have been measured at various energies (see Dermer 1986 and Murphy et al. 1987). For the pion angular and energy distributions in these reactions we have used the double polynomial approximations of the experimental distributions at different incident proton energies presented in Barashenkov, Gudima, & Toneev (1969). For the p–α reaction we have used pion production cross sections from Gueglenko et al. (1990b), which are quite close to those given in Murphy et al. (1987), differing only at energies greater than 1 GeV. In this energy range there is only one laboratory measurement, at 1.408 GeV/nucleon, obtained at JINR, Dubna (Glagolev et al. 1977; V. Glagolev 1985, private communication), which provides the total cross section as well as the pion angular and energy distributions. In Mandzhavidze (1987) these distributions were calculated at various energies, using an internuclear cascade code. The results of these calculations are in a good agreement with the experiment at 1.408 GeV/nucleon, and they allow to represent angular distributions and energy spectra of pions in different directions as polynomials of incident proton energy. The coefficients of these polynomials are given in Gueglenko et al. (1990b).

Next we consider the generation of the gamma rays. Neutral pions decay directly into two gamma quanta whose angular distribution is isotropic in the rest frame of the neutral pion. Positive pions decay into positrons via $\pi^+ \rightarrow \mu^+ \rightarrow e^+$. We use the differential cross sections for muon decay from Okun (1982) to obtain the angle and energy of the produced positrons. We ignore the negatively charged pions, as their contribution is only a few percent of that of the positive pions (Murphy et al. 1987).

We treat the transport of the positrons in the loop by taking into account the Coulomb, synchrotron losses, and bremsstrahlung energy losses, the removal of positrons due to annihilation in flight, mirroring in the convergent magnetic flux tube, and pitch-angle scattering by the same spectrum of Alfvén waves as that which scatters the ions. An important difference between the positron and ion transport is the fact that the positrons are produced predominantly in the chromosphere and photosphere, whereas the ions are assumed to be injected at the top of the loop. As the positrons slow down, they produce bremsstrahlung and annihilation photons in flight. We assumed that the bremsstrahlung is produced in a hydrogen plasma and used the differential bremsstrahlung cross sections from Ginzburg (1984). Bremsstrahlung is produced in the nonscreened regime if the interaction occurs in the ionized corona. In the neutral region below the transition, photons are produced in the nonscreened regime if their energy is greater than $E_{\rm crit} = E^2/(E + m_e c^2/\alpha)$, and in the screened regime otherwise. Here E is the energy of the positron, and α is the fine-structure constant. Since we consider only the high-energy gamma rays produced by ultrarelativistic positrons, we assume that both the bremsstrahlung and the high-energy annihilation photons are emitted in the direction of motion of the incident positron. The other photon resulting from annihilation in flight is emitted at low energies and is ignored here.

We also take into account the effects of Compton scattering and pair production on the transport of the gamma rays in the solar atmosphere. As the pions are produced quite deep into the atmosphere, these effects introduce important modifications to the flux and spectrum of the escaping gamma rays. Pair production by gamma rays, however, contributes no more than 20% of the total amount of secondary electrons and positrons generated by pion decay. Moreover, these pairs are mostly directed toward the Sun and have, on the average, smaller energies than the pion decay electrons and positrons. Therefore, their contribution to the escaping high-energy radiation can be neglected.

3. NUMERICAL RESULTS

The Monte Carlo simulations described in the previous section allow us to obtain distributions which can be com-

pared to the observations. We consider the depth distribution and time profile of the pion and gamma-ray production, and the angular distribution and energy spectra of the escaping radiation. Our main modeling parameters are: the following index γ of the energy spectrum of the primary accelerated particles; the loop radius R; the ambient coronal gas density n_c; the magnitude of the coronal magnetic field B_c; the mirror ratio B_{ph}/B_c; the total energy density in Alfvén turbulence W_{tot} (which is reflected in the computational parameter λ); and the density scale height h_a of the atmosphere below the transition. For the numerical results presented in the various figures, if not specifically indicated, the loop radius $R = 10^9$ cm, coronal magnetic field $B_c = 100$ G, and $n_c = 10^{10}$ cm^{-3}. All the calculated curves are normalized such that $N_p(>30$ MeV$) = 1$, where $N_p(>30$ MeV) is the total number of injected protons of energies greater than 30 MeV.

In Figure 1 we show the depth distributions of π^0 production below the transition in the case with no pitch-angle scattering for different values of the mirror ratio and two values of h_a. We consider first the curves for $h_a = 200$ km. The depth distribution of the decay gamma rays is identical to that of the pions because of the very short lifetime of the neutral pions. Pion production around the peaks at $z \approx 2000$ km and at larger depths is mostly due to particles in the loss cone, whereas the production at lower values of z is predominantly due to particles with larger pitch angles which mirror many times. In the case of strong convergence ($B_{ph}/B_c = 10$), the contribution of the mirroring particles is larger than that of the particles in the loss cone, while for the case of weak convergence ($B_{ph}/B_c = 1.01$) the opposite is true. We also present in Figure 1 the depth distribution calculated for an atmospheric model with a smaller value of h_a. In both models the ambient gas density at the edge of the photosphere ($z = 2000$ km) is the same, but for $h_a = 120$ km the density in the upward direction decreases much faster than for $h_a = 200$ km. This is the reason for sharp drop of the production at low values of z for the smaller scale height. On the other hand, in this case the density increases more rapidly below the photosphere, preventing the particles from penetrating as deeply as in the case of $h_a = 200$ km.

Figure 2 shows the effect of the pitch-angle scattering on the depth distribution of π^0 production. As compared to the unscattered case, pions are now produced by particles which on the average have smaller pitch angles and can penetrate deeper before mirroring. This leads to the decrease of the production in the upper chromosphere and to the almost total suppression of the coronal production. We can also see that, as in the case of no pitch-angle scattering, the depth distributions depend on the value of h_a. In both the scattered and unscattered cases, pion production due to particles in the loss cone peaks at the boundary between the chromosphere and photosphere ($z \approx 2000$ km), corresponding to a total grammage for the overlying atmosphere of about 10 g cm^{-2}. This should be compared with the depth profile of nuclear line production (Hua et al. 1989). Here the production due to particles in the loss cone peaks at higher altitudes, corresponding to a grammage of about 0.1 g cm^{-2}. This difference is due to the fact that the effective energies of the protons and α-particles which produce pions are much higher than those of the particles which produce the gamma-ray lines.

In addition to the pion production below the transition (shown in Figs. 1 and 2) there is also production in the corona. In Table 1 we show the fraction of pions produced in the coronal part of loop. Except for the values in parentheses, brackets, and braces, the results were obtained for $\gamma = 3$, $n_c = 10^{10}$ cm^{-3}, $R = 10^9$ cm, $B_c = 100$ G, and $h_a = 200$ km. In the case of no pitch-angle scattering ($W_{tot} = 0$), the fraction depends on the mirror ratio, decreasing from a high value of about 44% in the case of the highest convergence that we have considered to less than 1% for $B_{ph}/B_c = 1.01$. The coronal fraction also depends on the atmospheric model and the loop radius, as can be seen from the table. However, when pitch-angle scattering is taken into account, the coronal fraction is much smaller and becomes totally negligible for some parameters.

In Figure 3 we show the depths distributions of π^+ pro-

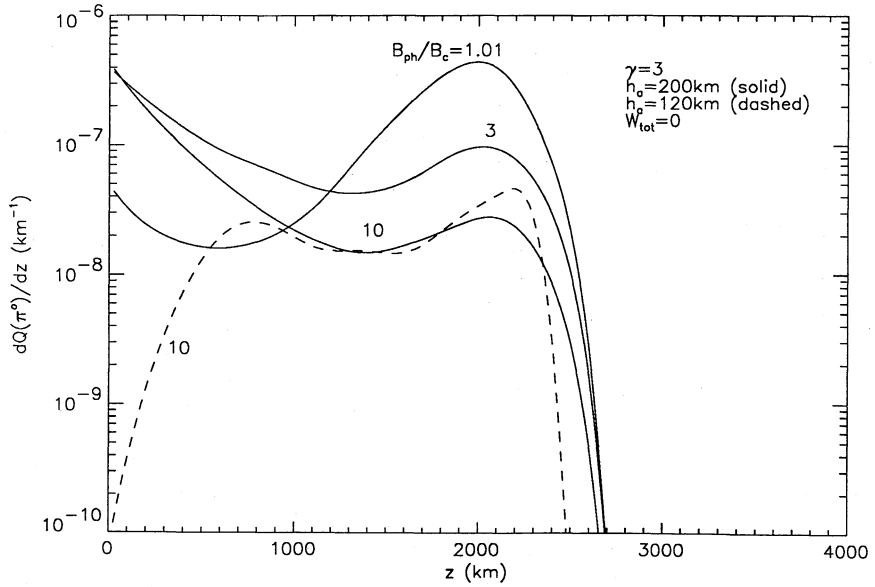

FIG. 1.—Depth distributions of the π^0 production for various values of the magnetic field convergence and the atmospheric scale height in the absence of pitch-angle scattering. The curves are normalized such that $N_p(>30$ MeV$) = 1$.

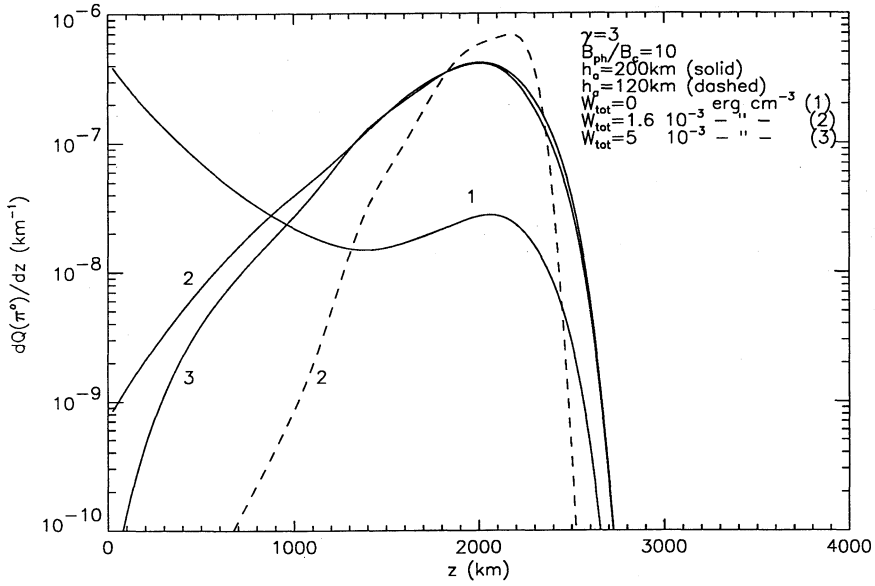

FIG. 2.—Depth distributions of the π^0 production for various values of the total turbulent energy density and the atmospheric scale height; $N_p(>30\ \text{MeV}) = 1$

TABLE 1

FRACTION OF π^0 PRODUCTION IN THE CORONA

	W_{tot} (ergs cm^{-3})		
B_{ph}/B_c	0	1.6×10^{-5}	1.6×10^{-3}
30.....	0.44	0.022	0.002
10.....	0.22	0.012	0.00015
	[0.77]	[0.017]	[0.00033]
	(0.34)	(0.054)	(0.0012)
	{0.34}	{0.061}	{0.00076}
3.....	0.08	0.0035	0.0
1.01	0.004	0.0	0.0

NOTES.—Brackets—$h_a = 120$ km; parentheses—$R = 10^{10}$ cm; and braces—$n_c = 10^{11}$ cm^{-3}.

duction and the depth distributions of the gamma rays resulting from the bremsstrahlung and annihilation in flight of the positrons from the decay of these pions. Here, in addition to the transport of the ions which produce the pions, we have also taken into account the transport of the secondary positrons. The general properties of these distributions are similar to those of the π^0 distributions discussed above.

We now turn to the time profiles of radiations. In Figure 4 we show the π^0 production rates for different values of the mirror ratio and no pitch-angle scattering, while in Figure 5 we show these rates for constant B_{ph}/B_c and different values of the total energy density of Alfvén turbulence, W_{tot}. In both cases the first peak occurs at the time when relativistic protons released at the top of the loop with pitch angles close to 0° hit the photosphere. Particles with larger pitch angles can mirror back

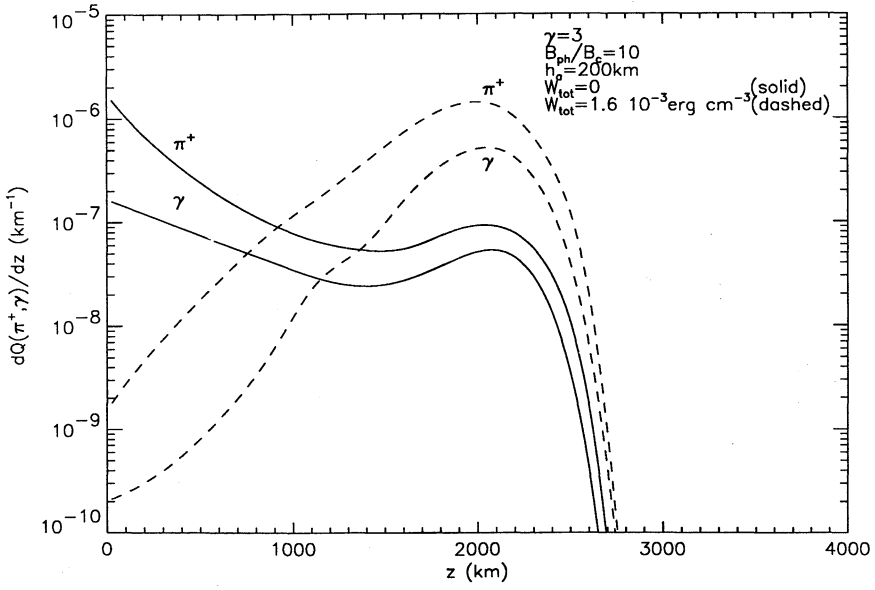

FIG. 3.—Depth distributions of the π^+ production and π^+ decay gamma-ray production for the two limiting cases of no pitch-angle scattering and strong pitch-angle scattering; $N_p(>30\ \text{MeV}) = 1$.

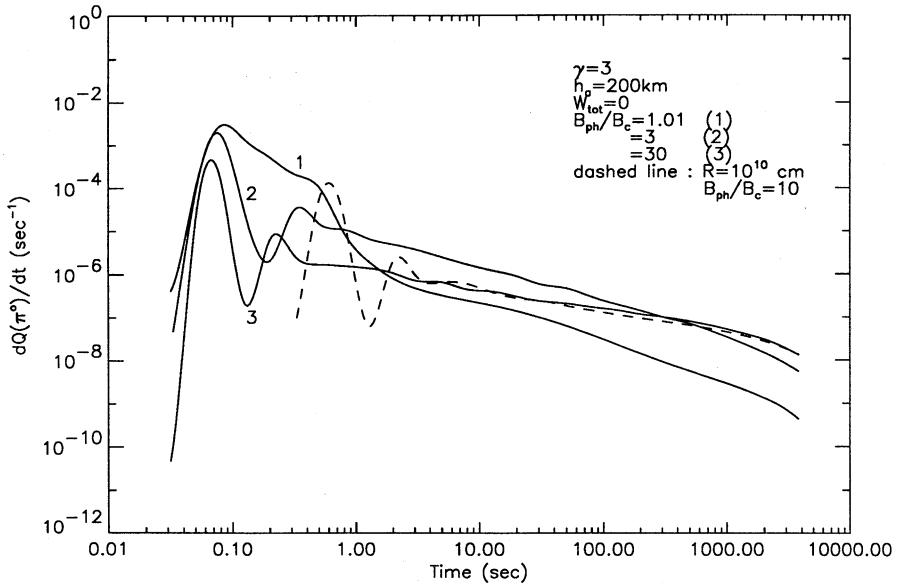

FIG. 4.—Time dependence of the π^0 production for various values of the magnetic field convergence and two values of the loop radius in the absence of pitch-angle scattering; $N_p(>30\,\mathrm{MeV}) = 1$.

and forth many times before they lose their energy, leading to pion production over an extended time period. The decrease of convergence, as well as pitch-angle scattering, are both causing the increase of the effective grammage to the mirror point, and hence the faster decline of the time profiles. The dashed curve in Figure 4 corresponds to the larger loop length, $R = 10^{10}$ cm. Due to the longer transport time of the particles through the loop, the first peak is shifted to a later time, and the time profile becomes more extended. We see that time profile of the production for $R = 10^{10}$ cm and $B_{ph}/B_c = 10$ is as extended as that for the stronger convergence ($B_{ph}/B_c = 30$) but shorter loop length ($R = 10^9$ cm). In Figure 5 we also show that time profiles for the atmospheric model characterized by $h_a =$ 120 km. In the case of strong pitch-angle scattering, when essentially all the production is in the lower chromosphere and photosphere, the variation in h_a has almost no effect on the time profiles. In the case of no pitch-angle scattering, the shorter atmospheric scale height reduces the chromospheric production relative to the coronal production (see Fig. 1 and Table 1), leading to a more extended time profile.

The decline of the time profiles is fastest when the pitch-angle scattering rate ν is at saturation. This rate can be estimated by equating the particle transit time through the loop to the diffusion time across the loss cone half-angle α_c (Miller & Ramaty 1989; Hua et al. 1989), $\alpha_c^2/\nu \approx \pi R/v$, where ν is the scattering rate equal to $D_{\mu\mu}/(1-\mu^2)$ evaluated at $\mu = 1$. The characteristic decay time of the radiation in the saturated regime can be estimated from the formula $\tau_s = \tau_0/(1 - \cos\alpha_c)$, where $\tau_0 = \pi R/(v \times \cos\alpha_c)$ is the transit time of particles in the loss cone through the loop. For the assumed atmospheric

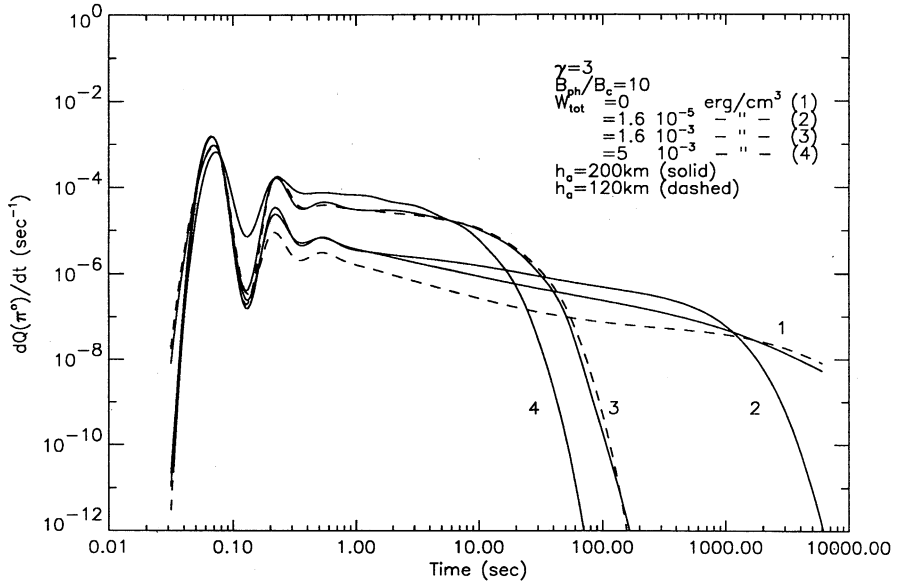

FIG. 5.—Time dependence of the π^0 production for various values of the total turbulent energy density and the atmospheric scale height; $N_p(>30\,\mathrm{MeV}) = 1$

model with $h_a = 200$ km and $B_{ph}/B_c = 10$, we find that cos α_c approximately equals 0.95, where we took the characteristic energy of the pion-producing particles to be about 700 MeV/nucleon. For $R = 10^9$ cm, $\tau_s = 3$ s. Using the equations given in the previous section, we obtain that at saturation $W_{tot} \approx 4.9 \times 10^7 \alpha_c^2/R$ ergs cm^{-3} $\approx 5.0 \times 10^{-3}$ ergs cm^{-3} for $R = 10^9$ cm. In Figure 5 the curve corresponding to $W_{tot} = 5.0 \times 10^{-3}$ ergs cm^{-3} after a few tenths of seconds can be well approximated by an exponential with characteristic decay time 3.7 s, which is close to the above estimate. The decay time at saturation increases proportionally to the loop length, and it also depends on the mirror ratio, which determines the size of the loss cone. For $B_{ph}/B_c = 3$ and $B_{ph}/B_c = 30$ the cosine of the loss cone half-angles are 0.81 and 0.98, respectively, yielding characteristic decay times of ≈ 1 s and 6.5 s for a loop radius of 10^9 cm.

The production rates of charged pions and the gamma rays resulting from their decay are shown in Figure 6. We see that in both the scattered and unscattered cases the time profiles of the gamma rays are quite similar to those of the pions. This is quite obvious in the case of pitch-angle scattering, where, as discussed above, the gamma rays are produced close to the production site of the pions. In the case of no pitch-angle scattering, the positrons undergo significant transport after their production, but the time required for this transport is short relative to the transport time of the primary ions. Again, similar to the case of neutral pions, there is extended production in the absence of scattering, and a rapid exponential decay caused by strong scattering. We also show in the figure the production rates of the gamma rays calculated for the smaller value of the coronal magnetic field $B_c = 20$ G. In the case of no scattering, the reduction of the magnetic field decreases the synchrotron losses and hence increases the lifetimes of the positrons in the loop. This leads to a more extended gamma-ray time profile, as well as to an increase in the total gamma-ray yields by about factor of 1.4 compared to the similar case with $B_c = 100$ G. However, in the case of the strong scattering, the lifetime of the positrons is very short due to the fast precipitation through the loss cones. Therefore, in this case the synchrotron losses are less important, and the calculated time profiles for different values of B_c are almost identical (we do not show in the figure the curve corresponding to $B_c = 20$ G). For the ions, the synchrotron losses are negligible, and therefore the production rates of pions and of π^0 decay gamma rays do not depend on the value of B_c.

We now consider the angular distribution of the radiations. Pion production in nuclear reactions, especially at high energies, is anisotropic, peaking in the direction of motion of the incident fast particle. Although the decay of the neutral pions into two photons partially isotropizes the angular distribution of the gamma radiation, this preferential direction of emission is still preserved. In Figure 7 we show the angular distributions of the produced and escaping gamma rays from π^0 decay for no pitch-angle scattering and two values of B_{ph}/B_c. The angle ψ is measured from the upward vertical direction. We see that the angular distribution of the produced radiation depends on the mirror ratio (compare the solid and dashed curves). When $B_{ph}/B_c = 1.01$, the effects of mirroring are small, and the radiation is mostly produced by downward-moving particles and hence significantly peaked in this direction. As we already have seen, pions in this case are produced deep in the solar atmosphere. Consequently, the escaping radiation is strongly attenuated, especially in the direction tangential to the photosphere. In the case of stronger convergence, the probability of pion production is maximal at the mirror point, where the incident particles move parallel to photosphere, resulting in a maximum at cos $\psi = 0$. Attenuation in this case is insignificant, because the gamma rays are produced higher in the atmosphere. In fact, we see that close to cos $\psi = 0$, instead of being attenuated, the escaping radiation exceeds the production. This effect is due to the additional flux of backscattered photons which were initially emitted in the downward direction. The angular distributions also depend on the assumed atmospheric scale height (compare the solid and dashed-dotted curves). We see that for the smaller atmospheric scale height ($h_a = 120$ km) there is almost no directivity of

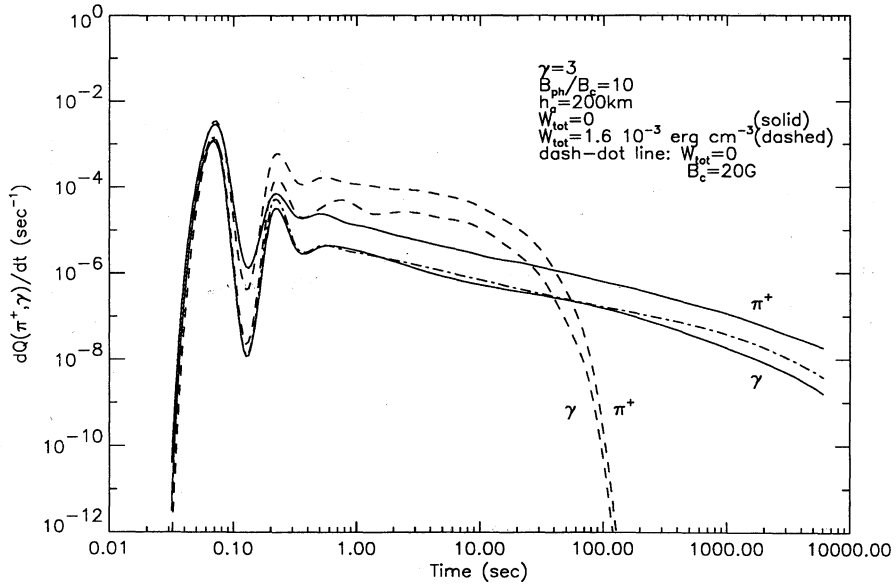

FIG. 6.—Time dependence of the π^+ production and π^+ decay gamma-ray production for the two limiting cases of no pitch-angle scattering and strong pitch-angle scattering. For all curves, except the dashed-dotted curve, the control magnetic field is 100 G; $N_p(>30$ MeV$) = 1$.

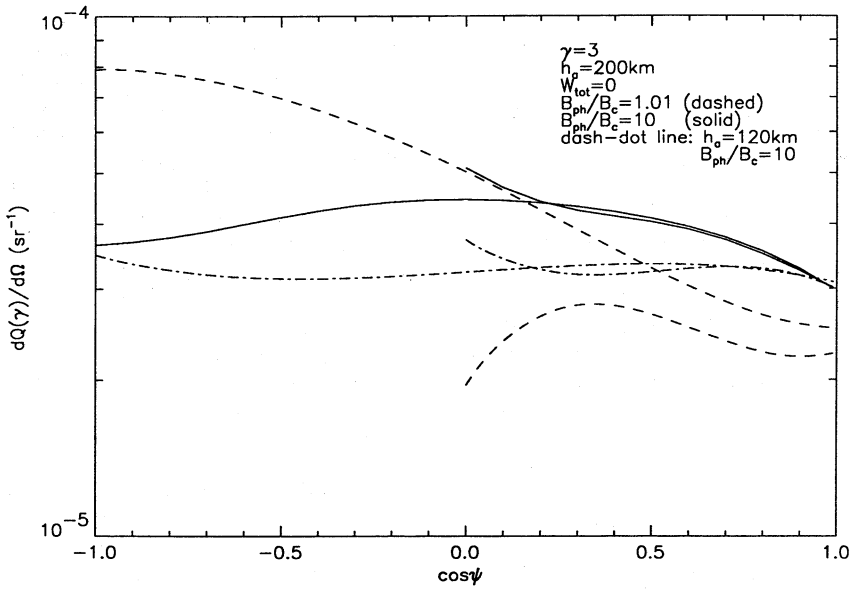

FIG. 7.—Angular distributions of produced and escaping π^0 decay gamma rays for various values of the magnetic field convergence and the atmospheric scale height in the absence of pitch-angle scattering. The angle ψ is the angle between an upward-directed solar radius vector and the direction of observation. The curves limited to positive values of cos ψ show the escaping photon distributions; $N_p(>30\ \mathrm{MeV}) = 1$.

radiation, due to the high fraction of isotropic emission produced in the coronal part of the loop (see Table 1).

In Figure 8 we present the angular distributions of gamma rays from π^0 decay for $B_{ph}/B_c = 10$ and the two limiting cases of no pitch-angle scattering and strong scattering. The distributions for strong scattering are similar to those obtained for the very small mirror ratio in Figure 7, because the scattering increases the number of particles moving downward with small pitch angles which interact deep in the atmosphere. Radiation produced by these particles is directed mostly downward and is strongly attenuated during the propagation of the photons. We do not show here the angular distributions for $h_a = 120$ km and strong scattering, as these distributions are quite similar to those for $h_a = 200$ km and strong scattering (*dashed curves*). This is because in the case of strong scattering the pions are produced mostly in the low chromosphere and photosphere where the density profiles for the two choices of h_a are not very different.

The angular distributions of the produced and escaping radiations from π^+ decay for the unscattered and strongly scattered cases are shown in Figure 9. We see that these angular distributions are more anisotropic than those for π^0 decay shown in Figures 7 and 8. The increased anisotropy is due to the transport of the positrons and the strong directionality of bremsstrahlung and annihilation in flight at ultrarelativistic energies. Considering first the cases of no scattering (solid

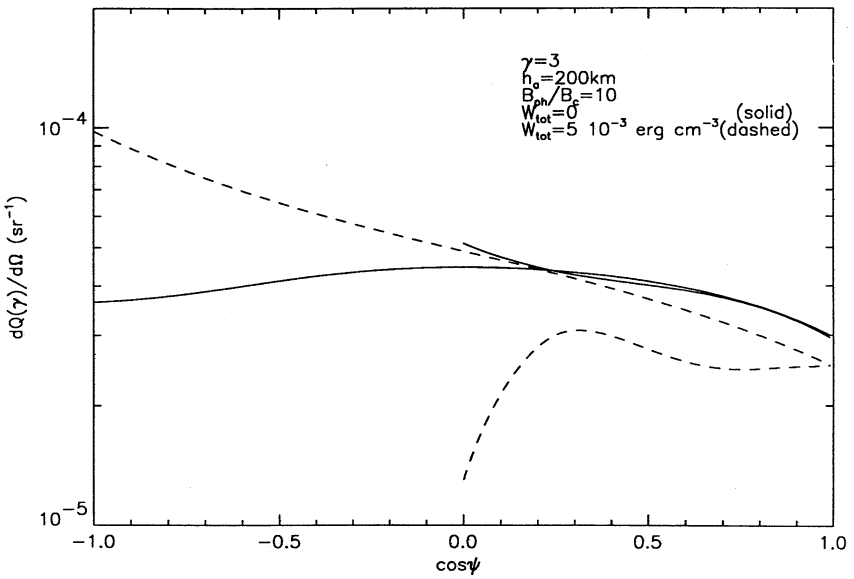

FIG. 8.—Angular distributions of produced and escaping π^0 decay gamma rays for the cases of no pitch-angle scattering and strong pitch-angle scattering. The curves limited to positive values of cos ψ show the escaping photon distributions; $N_p(>30\ \mathrm{MeV}) = 1$.

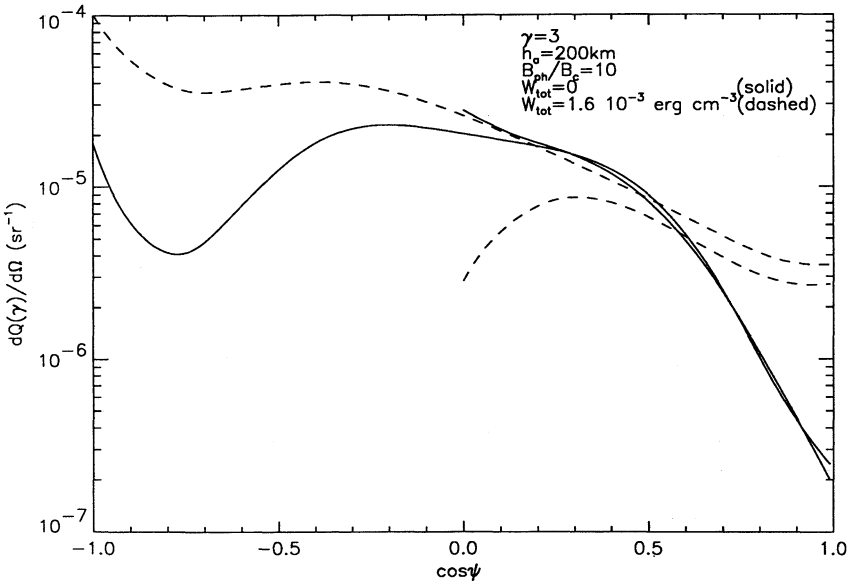

FIG. 9.—Angular distributions of produced and escaping π^+ decay gamma rays for the cases of no pitch-angle scattering and strong pitch-angle scattering. The curves limited to positive values of cos ψ show the escaping photon distributions; $N_p(>30\ \mathrm{MeV}) = 1$.

curves), we note the strong anisotropy in the backward direction, due to the mirroring of the positrons, and the fact that the attenuation of the escaping photons is small. The feature near $\cos\psi = -1$ is due to the focusing of the positrons. As we have seen above, most of the positrons are produced below the transition layer in a region of convergent magnetic field. The positrons that get out to the coronal part (either directly, or after mirroring) are strongly focused by the decreasing magnetic field. When these positrons reenter the dense regions of the atmosphere, they produce radiation predominantly in the downward direction. In the case of strong scattering, the positrons are produced deep in the atmosphere, and most of them lose their energy and emit photons before they can get out to the corona. Radiation in this case is more isotropic and also stronger attenuated, as can be seen from the figure.

The angular distributions of the total escaping greater than 10 MeV gamma-ray emission and its components are shown in Figure 10. It can be seen that in both the scattered and unscattered cases the radiation from the netural pions is dominant in all directions, although in the unscattered case the contribution of π^+ decays is important at directions close to $\psi = 90°$. In both cases the total radiation is slightly anisotropic. When there is no pitch-angle scattering, the emission is maximal in the direction $\psi = 90°$. However, in the case of strong scattering, the maximum is shifted to an angle in the range between 72° and 75°, due to the strong limb attenuation.

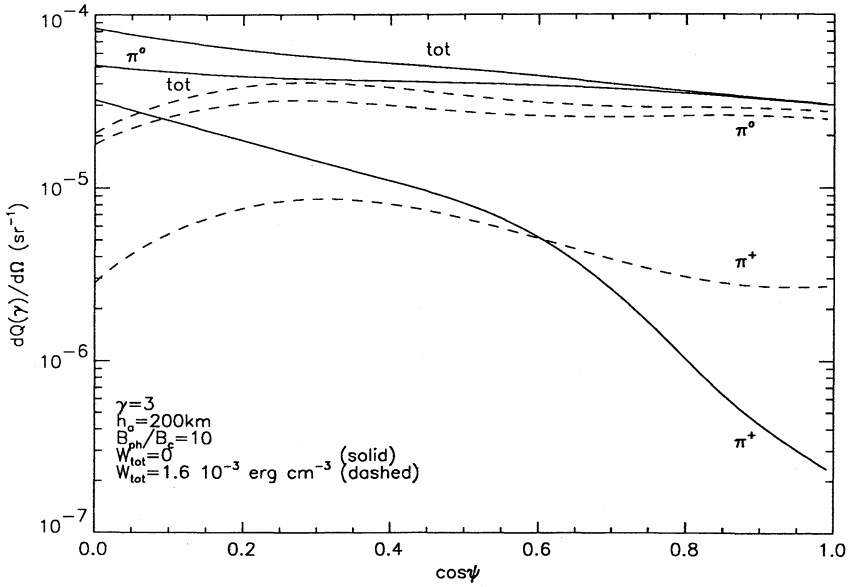

FIG. 10.—Angular distributions of the escaping π^0, π^+, and total pion decay radiation for the cases of no pitch-angle scattering and strong pitch-angle scattering; $N_p(>30\ \mathrm{MeV}) = 1$.

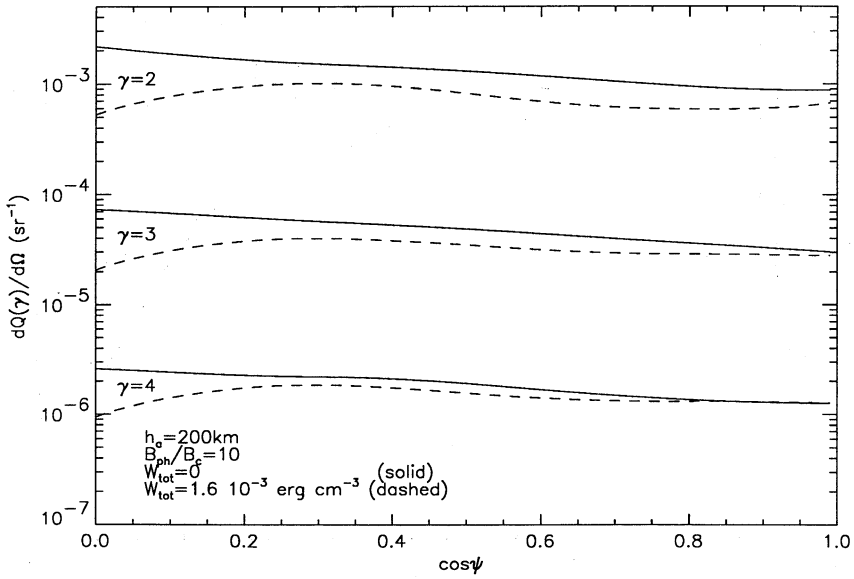

FIG. 11.—Angular distributions of the escaping total pion decay radiation for the cases of no pitch-angle scattering and strong pitch-angle scattering and various ion spectral indexes; $N_p(>30\ \mathrm{MeV}) = 1$.

The angular dependence of the total escaping gamma-ray emission greater than 10 MeV for various primary ion spectra is shown in Figure 11 for both the scattered and unscattered cases. We see that the angular distributions are essentially independent of the ion spectral shape. However, the total flux is very sensitive to the assumed spectrum of the ions.

In Figures 12 and 13 we show angle integrated energy spectra of the escaping radiation for the unscattered and scattered cases, respectively. In both cases the contribution from the neutral pions is dominant at high energies, while at lower energies the radiation comes mostly from π^+ decays. The contribution of π^+ is suppressed in our model relative to the previous results of Murphy et al. (1987). In the case of no pitch-angle scattering this suppression is caused by increased synchrotron energy losses of positrons trapped for considerable periods of time in the corona. In the scattered case, the suppression is caused by the strong attenuation of the escaping radiation. The attenuation of the π^+ component is stronger than that of the π^0 component. This is caused by the positron transport effects discussed above and also by the fact that the interaction cross sections of the π^+ decay photons (which have on the average smaller energies) are larger than those of the π^0 decay photons. Due to these suppressions, the total pion decay spectra are almost flat in the range 20–100 MeV, in contrast to the spectra presented by Murphy et al. (1987) which are considerably steeper. In Figure 14 we show the energy spectrum of the total escaping radiation for various primary ion spectra, in both the scattered and unscattered cases. We see that the shape

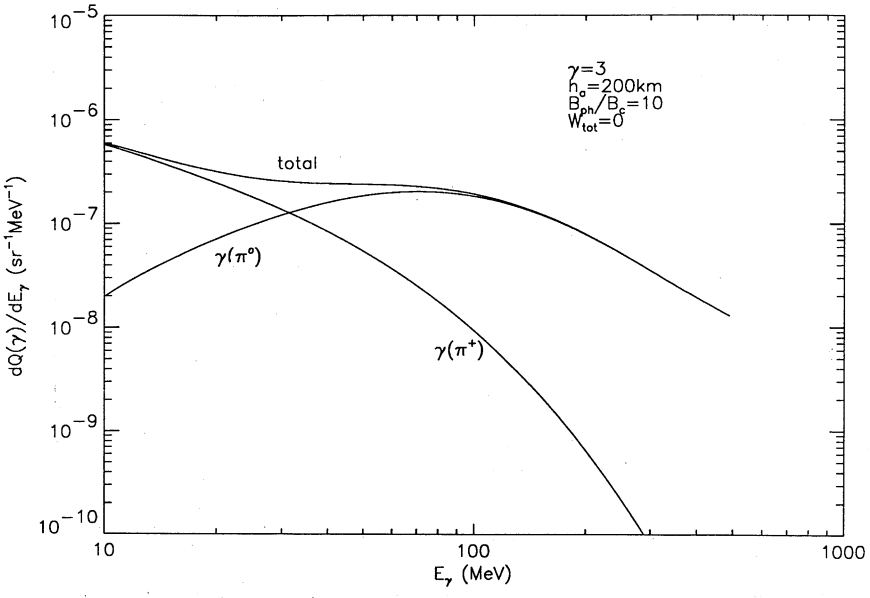

FIG. 12.—Angle integrated energy spectra of the escaping π^0, π^+, and total pion decay radiation in the absence of pitch-angle scattering; $N_p(>30\ \mathrm{MeV}) = 1$

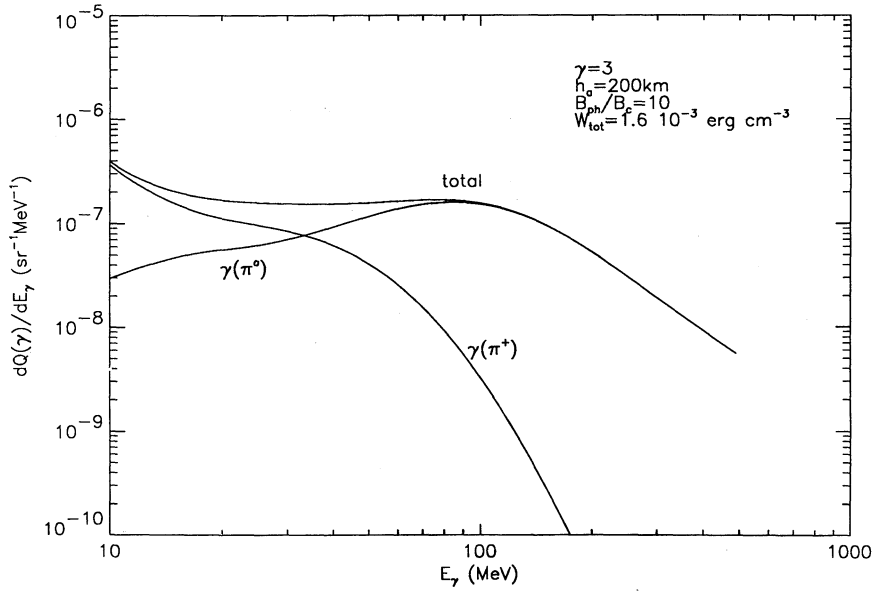

FIG. 13.—Angle integrated energy spectra of the escaping π^0, π^+, and total pion decay radiation in the case of strong pitch-angle scattering; $N_p(>30\ \mathrm{MeV}) = 1$

of the ion spectrum does not significantly affect the gamma-ray spectra, except at high energies (>100 MeV), where a harder ion spectrum produces a harder photon spectrum.

Finally, in Figure 15 we show directional energy spectra of total pion decay emission in three angular intervals. We see that when there is no pitch-angle scattering, the spectra strongly depend on the direction of observation. In particular, in the upward direction (curve 3) the contribution of the π^+ component is suppressed because of the stronger directivity of this component than that of the π^0 component (see Fig. 10). On the other hand, in the case of strong pitch-angle scattering, the dependence of the spectra on the emission direction is less pronounced because the radiation pattern of the π^+ component is approximately similar to that of the π^0 component (see Fig. 10). Since the angular distribution of the interacting ions in this case of strong scattering is peaked in the downward direction, the π^0 component observed in the upward direction is slightly redshifted, resulting in a softer spectrum at the high energies. Similar redshifts were shown by Miller (1990) employing a thick target model with assumed ion angular distributions.

4. DISCUSSION

Gamma-ray emission above 10 MeV was detected from 25 flares with the *SMM*/GRS (Rieger et al. 1983; E. Rieger 1991, private communication). However, in only one case, that of the flare of 1982 June 3, were the gamma rays produced by primary electron bremsstrahlung clearly separated from those

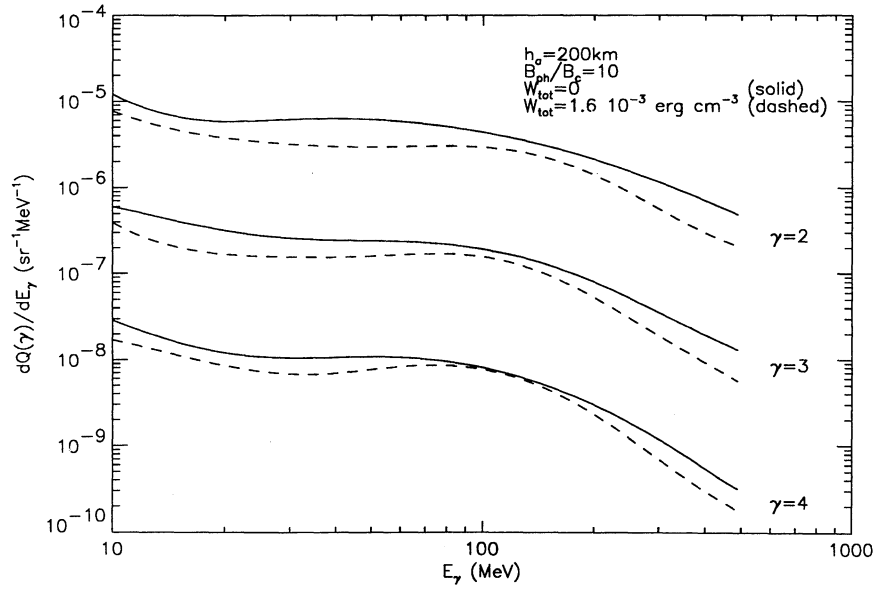

FIG. 14.—Angle integrated total energy spectra of the escaping pion decay radiation for the cases of no pitch-angle scattering and strong pitch-angle scattering, and various values of the ion spectral index; $N_p(>30\ \mathrm{MeV}) = 1$.

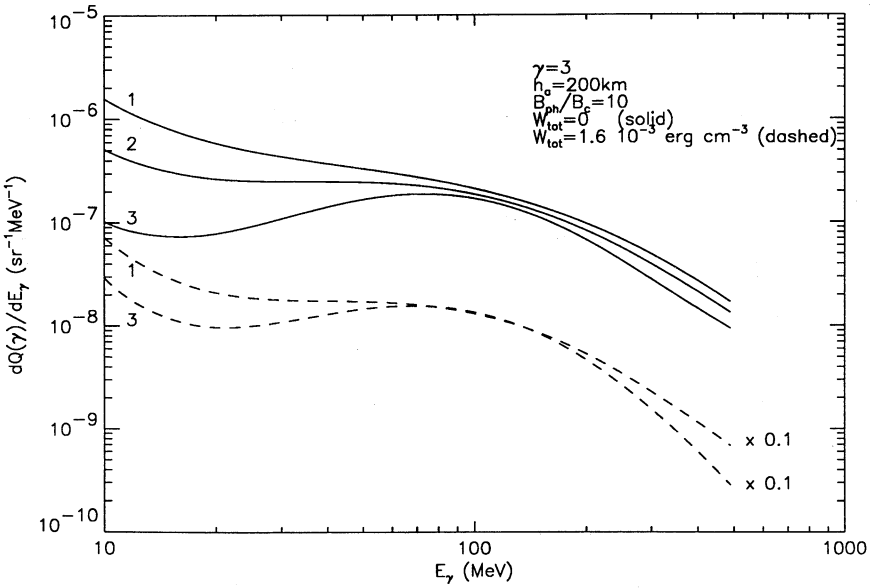

FIG. 15.—Directional energy spectra of the total pion decay emission for no pitch-angle scattering and strong scattering. *Line 1:* $0 < \cos\psi < 0.33$; *line 2:* $0.33 < \cos\psi < 0.67$; *line 3:* $0.67 < \cos\psi < 1.0$; $N_p(>30\ \text{MeV}) = 1$.

resulting from pion decay (Forrest et al. 1986). There is at least one more flare (1984 April 24) with strong evidence of pionic emission (D. J. Forrest 1988, private communication). In addition, there are several other flares with marginal evidence for pion radiation (E. Rieger 1991, private communication). In the present section we first apply our calculations on the angular distribution of pion radiation to the observed distribution of flares on the Sun. Next, we consider the time dependence and the energy spectrum of pion radiation observed from the 1982 June flare and compare these data with our calculations.

4.1. *Angular Distributions*

In Figure 16 we plot the longitude distribution of 25 flares with gamma-ray emission greater than 10 MeV, with the flares grouped in three longitude intervals. We have calculated theoretical longitude distributions resulting from our model, assuming that the integral flare size distribution is inversely proportional to the flare size (Dermer & Ramaty 1986) and that the flares on the Sun are uniformly distributed between heliolatitudes $\pm 40°$. Since the calculated angular distributions shown in Figure 11 for various ion spectral shapes are quite similar, in Figure 16 we only show results for $\gamma = 3$. We have integrated the theoretical curves over the three longitude intervals, and we have normalized the calculations to the data by minimizing χ^2. We find that the case of no pitch angle scattering and $h_a = 200$ km can be rejected at the 92.5% confidence level. The case of strong pitch-angle scattering, as well as the case of no pitch-angle scattering with the smaller atmospheric

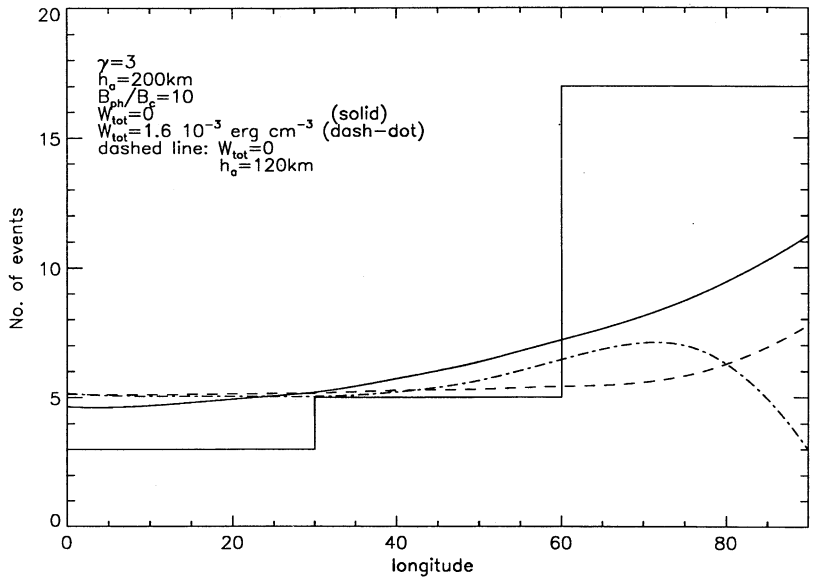

FIG. 16.—Heliolongitude distribution of solar flares with detected >10 MeV radiation (histogram, E. Rieger 1991, private communication). The curves are calculated heliolongitude distributions of flares with pion decay emission obtained for the various model parameters.

scale height (h_a = 120 km), both of which yield more isotropic distributions, can be rejected at the 98.5% level. It should be noted, however, that these results are valid only if the available sample of flares with greater than 10 MeV emission is an unbiased sample, unaffected by the fact that the *SMM*/GRS is triggered by emission greater than 300 keV and not by emission greater than 10 MeV. But it seems to us that this effect cannot bias the sample in any significant way, because the flares observed at energies greater than 10 MeV are in general intense at lower energies, so that it is quite unlikely that any significant number of greater than 10 MeV flares were missed because of the *SMM*/GRS triggering criteria.

Thus, pion decay radiation is probably not sufficiently anisotropic to account for the limb brightening of solar flare high-energy gamma rays. Our conclusion is the same as that of Gueglenko et al. (1990b), who considered only the radiation from neutral pions. Even though the gamma rays produced by secondary positrons contribute significantly to the total emission in the greater than 10 MeV energy range, and in some cases can increase the anisotropy, the effect is not sufficiently large to make the pionic interpretation of the high-energy gamma-ray emission from the solar flares plausible. On the other hand, as has been shown by Semukhin & Kovaltsov (1985), Miller & Ramaty (1989), MacKinnon & Brown (1989), and Kocharov & Kovaltsov (1990) the angular distribution of bremsstrahlung produced by primary electrons trapped in the magnetic loop is consistent with the observed longitudinal distributions of the flares.

From Figure 11 it follows that if there is no pitch-angle scattering, the most favorable flare position to observe pion emission is at the solar limb, as the same flare would produce about 2.5 times more emission from the limb than from disk center. However, in the regime of strong scattering, pion radiation from the limb is attenuated by about factor of 5, making it difficult to observe pion emission from limb flares. This could have been the reason that pion radiation was not seen during the 1980 June 21 flare (Forrest et al. 1985) from which high-energy neutrons were observed (Chupp et al. 1982). Another argument in favor of strong pitch-angle scattering of the trapped ions and electrons in this flare has been given by Hua et al. (1989) and Miller & Ramaty (1989), who suggested that the rapid decays of the two pulses of nuclear gamma-ray line emission and bremsstrahlung require pitch-angle scattering at a level close to saturation. On the other hand, the absence of pion radiation in the 1980 June 21 flare could have simply been the consequence of a steep ion spectrum for which pion production is negligible (Ramaty et al. 1983; Gueglenko et al. 1990b).

4.2. *Time Profiles, Energy Spectra, and Models for the 1982 June 3 flare*

The time profile of the pion decay radiation observed from the 1982 June 3 flare is shown in Figure 17. We see the observed time profile exhibited a short first pulse, lasting for about 1 minute and containing about 20% of the total pion emission, which was followed by a longer second pulse lasting for over a thousand seconds. This time profile was quite different from that of either the nuclear deexcitation emission in the 4–7 MeV range or the primary electron bremsstrahlung, as for both of these components the bulk of the photons were emitted during the first pulse (Forrest et al. 1986; Chupp et al. 1987; see also Figure 5 in Ramaty et al. 1990). In particular, about 80%

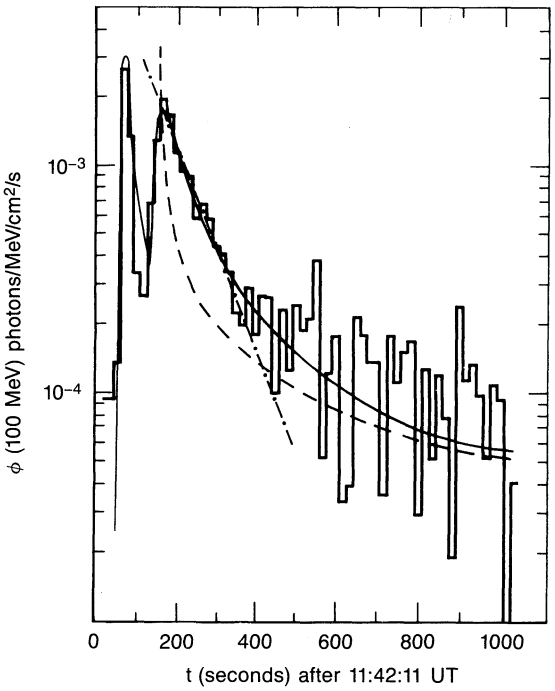

FIG. 17.—Time profile of the pion decay radiation, ϕ(100 MeV), observed from the 1982 June 3 flare (histogram from Ramaty et al. 1987, based on data of Forrest et al. 1986). The solid curve corresponds to unsaturated variable pitch-angle scattering rate with ion injection for 60 s during the first pulse. The time dependence of W_{tot} and the other parameters of the fit are given in the text. The solid curve limited to times after the second peak also represents the case of unsaturated variable scattering with injection at the second peak. The dashed and dashed dotted curves correspond to injection at the second peak and represent the cases of no pitch-angle scattering and saturated scattering, respectively. Except for W_{tot}, the parameters for the dashed curve are the same as for the solid curve.

of the total 4–7 MeV emission was observed during the first minute of the event. As has been emphasized by Murphy et al. (1987), the fact that the ratio of the flux in pion emission to that in nuclear line emission was much larger during the second pulse than during the first, indicates that the spectrum of the interacting ions became harder with time during the flare. Murphy et al. (1987) proposed that this hardening was due to second phase acceleration. They assumed an isotropic thick target model in which there is almost no delay between particle acceleration and interaction. Therefore, the fact that during the first pulse the interacting particles had a steeper spectrum than those interacting during the second pulse must mean different accelerated ion spectra for the two pulses. This is the origin of the second phase suggestion for this flare. We should note, however, that the interaction site in the Murphy et al. (1987) model had to be in a dense region of the solar atmosphere. Since isotropy was assumed in the model, either the particles were accelerated in this dense region (which is unlikely), or a mechanism had to be found to isotropize the particles after their transport from the acceleration to the interaction site. This mechanism, however, was not specified.

On the other hand, Gueglenko et al. (1990a, b) suggested that the difference between the two time profiles resulted from the long time scale of the pion emission expected in loop models with no or weak pitch-angle scattering. The characteristic decay time of the radiation in this case is much larger than

that of the de-excitation gamma-ray line emission or primary electron bremsstrahlung (Hua et al. 1989; Miller & Ramaty 1989). This is due to the fact that the pion-producing particles have much longer ranges, and consequently longer lifetimes in the loop, than the ions which produce the de-excitation line emission or the electrons which produce the bremsstrahlung. In the Gueglenko et al. (1990a, b) model there is no pitch-angle scattering until the onset of the second pulse. As a result, the pion radiation observed in the first pulse is due mainly to the GeV protons in the loss cone. Thus, since isotropy is assumed in the model, the bulk of the GeV protons remain trapped in the corona and available for pion production at later times. Pitch-angle scattering is turned on at the onset of the second pulse by the introduction of an external source of turbulence. This causes an increase in the dumping rate of all the trapped particles. But because of their shorter loss time in the absence of pitch-angle scattering, not too many low-energy protons remain at this time. In the resultant second pulse, therefore, pion radiation dominates.

However, it is probably unlikely that pitch-angle scattering is negligible during the first pulse, since very high levels of turbulence are expected to be present at the time of particle acceleration. Furthermore, even in the absence of external sources of turbulence, pitch-angle scattering could occur as a result of turbulence generated by the accelerated particles themselves, due to the development of a loss-cone instability (see Bespalov, Zaitsev, and Stepanov 1987; Smith & Brecht 1991). Here, we first present a modification to the model of Gueglenko et al. (1990a, b) which shows that it is possible to obtain a good fit to the observed time profile in a one-phase acceleration model with pitch-angle scattering during the first pulse. On the other hand, if the scattering rate during the first pulse was strong enough, all of the particles, including those which produce the pions, were dumped rapidly, requiring that the pion emission observed during the second pulse be produced by particles accelerated in a second phase. We discuss this possibility after considering the modified one-phase model.

In our modified one-phase model we inject all the particles at a steady rate during the first pulse for 60 s beginning at $t = 36$ s (see Fig. 17). We assume that in both the first and second pulses the turbulent energy density starts out at a high level ($W_{tot} = 1.6 \times 10^{-4}$ ergs cm^{-3}) and then decays with time. During the first pulse, the decay should be fast, because otherwise most of the particles would be rapidly dumped and too much pion decay radiation would be produced. To fit the time profile during the second pulse with the same loop parameters a longer decay time is required. The solid curve in Figure 17, which fits the data quite well, was calculated with a variable scattering rate, corresponding to the following time dependence of the turbulent energy density: $W_{tot} = 1.6 \times 10^{-4}$ exp $[-(t - 34)/20]$ for $36 < t < 146$ and $W_{tot} = 1.6 \times 10^{-4}/(0.1t - 13.6)$ for $t > 146$, where W_{tot} is in ergs cm^{-3} and t is in s. The other parameters of the fit are $B_{ph}/B_c = 10$, $B_c = 100$ G, $n_c = 10^{10}$ cm^{-3}, $R = 10^9$ cm, $N_p(>30\ \text{MeV}) = 1.7 \times 10^{33}$, and $\gamma = 3.4$. These values of N_p and γ simultaneously account for the total observed π^0 decay emission (55 photons cm^{-2} s^{-1}; Forrest et al. 1986) and 4–7 MeV de-excitation line emission (305 photons cm^{-2} s^{-1}; Rieger et al. 1983). We calculate the de-excitation line flux from Murphy & Ramaty (1984), as this emission is essentially isotropic and optically thin (Hua et al. 1989), and therefore practically independent of the details of the loop model. In addition, with the same parameters we obtain good fits to the high-energy neutron observations (Chupp et al. 1987).

In Figure 18 we show fits obtained in the one-phase model to the observed energy spectrum of the greater than 10 MeV radiation measured at a time when the radiation was mostly pionic (Forrest 1988). The solid curves are our calculated time-integrated energy spectra of pion decay radiations emitted in the range of heliocentric angle cosines $0.15 < \cos\psi < 0.45$, which includes the flare heliocentric angle cosine (the flare location was S09E72). We also show the total pion decay spectrum, calculated for the same parameters, except that $B_c = 10$ G (dashed curve). The decrease of the coronal magnetic field

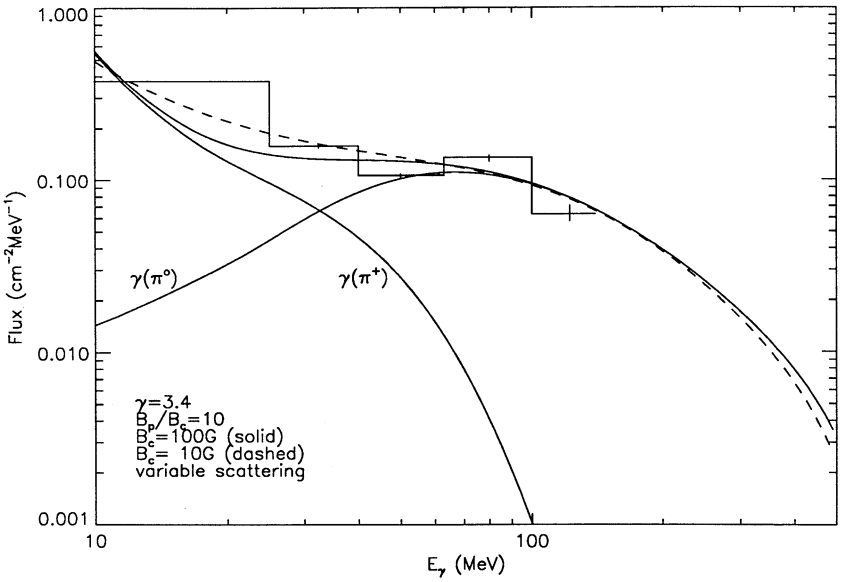

FIG. 18.—Histogram: energy spectrum of the greater than 10 MeV radiation observed (Forrest 1988) from the 1982 June 3 flare in the time interval 11:44:55 UT–11:47:06 UT (164–295 s in Fig. 17). The curves are calculated time-integrated directional ($0.15 < \cos\psi < 0.45$) pion decay gamma-ray spectra resulting from the one-phase acceleration model with variable pitch-angle scattering rate normalized to fit the data.

improves the fit, because it reduces the synchrotron losses of positrons and consequently increases the contribution of the π^+ component. The other components of the radiation do not depend on B_c and therefore remain unchanged. We see that a reasonably good fit to the observed spectrum can be obtained in this one-phase model.

In Figure 19 we show the time-integrated total pion decay spectra in the same interval of emission angles, calculated with a pitch-angle scattering rate which we now assume to be constant in time. The three curve represent the regimes of strong, weak, and no pitch-angle scattering. In the presence of pitch-angle scattering, the contribution of the π^+ component is suppressed relative to that of the π^0 component, due to its stronger attenuation (see § 3). As a result, the dashed and dotted curves do not provide good fits to the data. In the case of the weak scattering the fit can be improved by decreasing the value of coronal magnetic field, similar to the case of the variable scattering considered above. However, when there is strong scattering, the energy spectrum becomes practically independent of B_c, as most of the positrons precipitate rapidly before they experience significant synchrotron losses.

We return now to the two-phase acceleration model. The need for such a model arises if all of the particles, including those which produce the pions, are dumped during the first pulse due to strong pitch-angle scattering. Consequently, all the pion emission observed during the second pulse had to be produced by particles accelerated during this pulse. If this acceleration was impulsive (acceleration time much shorter than the duration of the pulse), then the long duration of the pulse ($\approx$1000 s) must have resulted from the trapping of the particle in the loop. We could fit the time profile shown in Figure 17 in the range 150–350 s with an exponential (dashed-dotted curve in Fig. 17), as expected for trapping with saturated pitch-angle scattering (§ 3). However, as we have just seen, saturated scattering does not provide a good fit to the observed energy spectrum in this time interval, and therefore can probably be ruled out. A better fit to both the time profile and energy spectrum during the declining portion of the second pulse can be obtained in the two-phase model with an unsaturated, variable pitch-angle scattering rate, similar to the scattering rate assumed in our one-phase model—except that in the two-phase model a new population of particles is injected at the peak of the second pulse with flatter spectrum than that of the particles injected in the first pulse. In this case, the time profile during the decline of the second pulse, as well as the energy spectrum, are fitted in essentially the same fashion as in the one-phase model (solid curve in Fig. 17 after $t = 164$ s, and dashed curve in Fig. 18). We see in Figure 19 that the calculated spectrum for $W_{tot} = 0$ does provide a good fit to the data. Nevertheless, this case of no pitch-angle scattering can be excluded because it produces a time profile which is not consistent with the observations (see dashed curve in Fig. 17). Thus, for the two-phase model, as well as for the one-phase model discussed above, the best explanation of the decay of the pion emission during the second pulse appears to be given by unsaturated, variable pitch-angle scattering. We note that Hua et al. (1989) found a good fit to the time profile of the 4–7 MeV de-excitation line emission during the second pulse between about 150 and 350 s with $W_{tot} = 1.6 \times 10^{-4}$ ergs cm^{-3}, and suggested that W_{tot} should decrease at later times. This also corresponds to unsaturated variable scattering.

There are several implicit assumptions in our above discussion. We have assumed that there is no extended acceleration during the second pulse. Such acceleration could eliminate the need for the decline of the turbulent energy density, and it could, in principle, explain the entire time profile with a very short trapping time resulting from either saturated pitch scattering or a loop geometry without magnetic field convergence. However, saturated scattering is still excluded because it does not provide a good fit to the energy spectrum, as we have shown above. This, however, is only true if we accept the experimental result that the observed energy spectrum is purely pionic during the 200 s after the peak of the second pulse, since an admixture of primary electron bremsstrahlung could improve the fit provided by the saturated scattering model (dashed curve in Fig. 19).

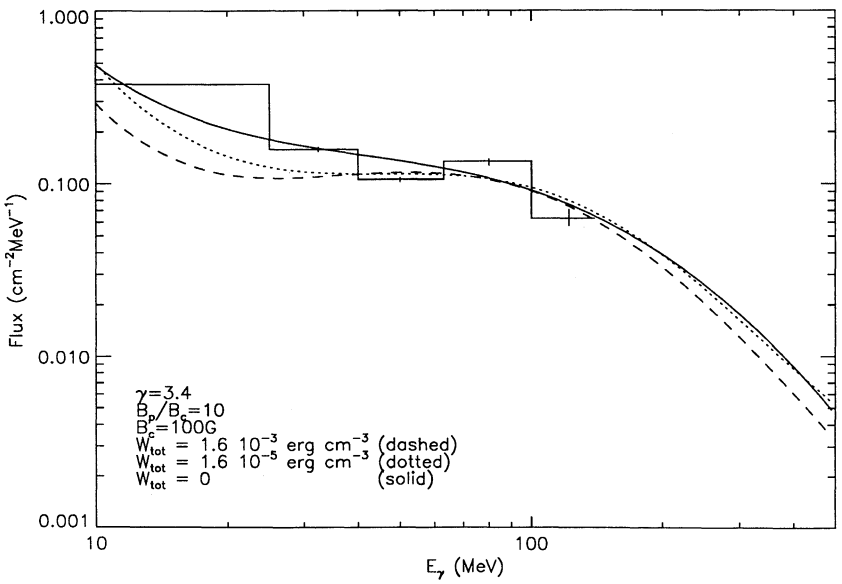

FIG. 19.—The same observed energy spectrum as in Fig. 18 compared with the theoretical time-integrated directional ($0.15 < \cos\psi < 0.45$) pion decay spectra calculated for the various turbulent energy densities. The curves are normalized to fit the data.

We should also mention that Ryan & Lee (1991) have suggested that the extended time profile of the pion emission in the 1982 June 3 flare could result from the trapping of ions in the coronal part of the loop by Alfvén turbulence. The energy density in this case is several orders of magnitude higher than the energy density required for saturated pitch-angle scattering. Ryan & Lee (1991) show that such a high-energy density will provide additional particle acceleration which will harden their energy spectrum during the diffusive propagation of the particles.

We have also assumed that all of the emissions are produced in a single loop. However, it is possible that the second pulse of emission was produced by particles trapped in a different loop, and furthermore that this emission was produced by particles accelerated outside of loops, for example by a shock moving through the corona (Murphy et al. 1987). Such models could be tested with data from imaging instruments which can resolve one loop from another. These observations could also distinguish between the case of a small emitting area associated with just a few loops from emission coming from a large fraction of the solar disk, as is expected if the acceleration is due to an extended coronal shock. In the case of a single loop, imaging observations could also resolve the pion emission produced in the corona from that produced below the transition. As we have seen in the § 3, the fraction of pions produced in the coronal part strongly depends on the parameters of the loop. it could be as high as 80% for some models (Table 1), but becomes negligible when the pitch-angle scattering is strong. Therefore, imaging observations of pion decay gamma rays with several arcsecond spatial resolution, capable of distinguishing between photospheric and coronal production could provide important information on the physical conditions in the flare loops.

5. SUMMARY

We have calculated distributions of pion production in a solar flare magnetic loop model as functions of atmospheric depth, time, emission angle, and photon energy. We found that if the mirror ratio is small, or if the rate of pitch-angle scattering in the corona is high, the bulk of the pions are produced deep in the atmosphere (lower chromosphere and photosphere). In these cases the escaping radiation is strongly attenuated, particularly for flares near the limb of the Sun. The time profiles of pion production strongly depend on the rate of pitch-angle scattering. They are very extended in the absence of scattering, but become quite impulsive when the scattering rate is near saturation. The angular distributions are moderately anisotropic, reaching maxima at directions tangential to the photosphere when there is no pitch-angle scattering and at emission angles (relative to the vertical upward direction) around 75° when there is a strong pitch-angle scattering. This anisotropy, however is not sufficiently high to account for the limb brightening of the solar flare greater than 10 MeV emission, showing that the bulk of this emission is bremsstrahlung of primary electrons. We also found that the spectrum of the pion emission depends on the direction of observation. In particular, in the upward direction the emission is suppressed at low energies and is redshifted at high energies.

We examined the models for the production of high energy photons in the 1982 June 3 flare, which exhibited two distinct pulses of pion emission. The one-phase acceleration model proposed by Kocharov et al. (1988) and Gueglenko et al. (1990a, b) requires no pitch-angle scattering or unsaturated variable scattering during the first pulse of the event and a sudden increase in the scattering rate at the beginning of the second pulse. The two-phase acceleration model proposed by Murphy et al. (1987) is needed if the turbulence during the first pulse is strong enough to precipitate the bulk of the particles on a short time scale. We find that time profile and energy spectrum of the pion emission observed during the decaying portion of the second pulse can be best explained with unsaturated variable pitch scattering, independent of whether the particles were injected during the first pulse or at a peak of the second pulse.

The results of our calculations show that future observations of the high-energy continuum emission from solar flares with high temporal, spatial, and energy resolution can provide important information on the physical conditions at the flare site. The predicted dependence of the spectrum of the pion radiation on the direction of observation could be observed by detecting high-energy emission from flares at different positions on the Sun, and the predicted overall anisotropy could be detected by stereoscopic observations with two or more spacecraft. In addition, to construct complete models of particle acceleration, transport, and interaction in flares like the 1982 June 3 flare, we need similar high-resolution observations of the other radiation components, particularly continuum emission of primary electrons, gamma-ray line emission at various energies, and neutrons.

We wish to acknowledge *SMM*/GRS data received from Erich Rieger prior to publication. We also wish to acknowledge D. J. Forrest for a useful discussion, and G. A. Kovaltsov and J. A. Miller for comments on the manuscript. Part of the research by N. M. was carried out as a visiting scientist at the Goddard Space Flight Center under the sponsorship of the US–USSR Solar Terrestrial Physics Working Group. She wishes to acknowledge the staff of the *SMM* Data Analysis Center, especially J. Gurman and R. Schwartz, for their hospitality and assistance.

REFERENCES

Avrett, E. H. 1981, in The Physics of Sunspots, ed. L. E. Cram & J. H. Thomas (Sacramento Peak Observatory: AURA), 235
Barashenkov, V. S., Gudima, H. K., & Toneev, V. D. 1969, Acta Phys. Polonicae, 36, 415
Bespalov, P. A., Zaitsev, D. V., & Stepanov, A. V. 1987, Sol. Phys., 114, 127
Chupp, E. L. 1984, ARA&A, 22, 359
———. 1990, Science, 250, 229
Chupp, E. L., et al. 1982, ApJ, 263, L95
———. 1987, ApJ, 318, 913
Dermer, C. D. 1986, ApJ, 307, 47
Dermer, C. D., & Ramaty, R. 1986, ApJ, 301, 962
Ellison, D. C., & Ramaty, R. 1985, ApJ, 298, 962
Forrest, D. J. 1988, in Nuclear Spectroscopy of Astrophysical Sources, ed. N. Gehrels & G. H. Share (New York: AIP), 211
Forrest, D. J., Vestrand, W. T., Chupp, E. L., Rieger, E., Cooper, J., & Share, G. 1985, Proc. 19th Internat. Cosmic Ray Conf. (La Jolla) (NASA CP-2376), 4, 146
———. 1986, Adv. Space Res., 6, No. 6, 115
Ginzburg, D. J. 1984, Cosmic Ray Astrophysics (Moscow: Nauka)
Glagolev, V. V., et al. 1977, preprint, JINR, Dubna, PI-10894
Gueglenko, V. G., et al. 1990a, ApJS, 73, 209
Gueglenko, V. G., Kocharov, G. E., Kovaltsov, G. A., Kocharov, L. G., & Mandzhavidze, N. Z. 1990b, Sol. Phys., 125, 91
Hua, X. M., Ramaty, R., & Lingenfelter, R. E. 1989, ApJ, 341, 516

Jokipii, J. R. 1966, ApJ, 146, 480
Kennel, C. F. 1969, Rev. Geophys., 7, 379
Kennel, C. F., & Petschek, H. E. 1966, J. Geophys. Res., 71, 1
Kocharov, G. E., Kovaltsov, G. A., Mandzhavidze, N. Z., Semukhin, P. E., & Kocharov, L. G. 1987, Proc. 20th Internat. Cosmic Ray Conf. (Moscow), 3, 74
Kocharov, G. E., Kocharov, L. G., Kovaltsov, G. A., & Mandzhavidze, N. Z. 1988, preprint, Acad. of Sciences of the USSR, A.F. Ioffe Physico-Technical Institute
Kocharov, L. G., & Kovaltsov, G. A. 1990, Sol. Phys., 125, 67
MacKinnon, A. L., & Brown, J. C. 1989, A&A, 215, 371
———. 1990, A&A, 232, 544
Mandzhavidze, N. Z. 1987, Ph.D. thesis, A. F. Ioffe Physico-Technical Inst., Leningrad, USSR
Miller, J. A. 1990, Ph.D. thesis, Univ. Maryland, College Park
Miller, J. A., & Ramaty, R. 1989, ApJ, 344, 873
Murphy, R. J., Dermer, C. D., & Ramaty, R. 1987, ApJ, 63, 721
Murphy, R. J., & Ramaty, R. 1984, Adv. Space Res., 4, No. 7, 127
Okun, L. B. 1982, Leptons and Quarks (Amsterdam: North-Holland)
Palmer, I. D., & Jokipii, J. R. 1981, Proc. 17th Internat. Cosmic Ray Conf. (Paris), 3, 381
Petrosian, V. 1985, ApJ, 299, 987
Ramaty, R. 1979, in Particle Acceleration Mechanisms in Astrophysics, ed. J. Arons, C. Max, & C. McKee (New York: AIP), 135
Ramaty, R., Miller, J. A., Hua, X. M., & Lingenfelter, R. E. 1988, in Nuclear Spectroscopy of Astrophysical Sources, ed. N. Gehrels & G. H. Share (New York: AIP), 217
———. 1990, ApJS, 73, 199
Ramaty, R., & Murphy, R. J. 1987, Space Sci. Rev., 45, 213
Ramaty, R., Murphy, R. J., & Dermer, C. D. 1987, ApJ, 316, L41
Ramaty, R., Murphy, R. J., Kozlovsky, B., & Lingenfelter, R. E. 1983, ApJ, 273, L41
Rieger, E. 1989, Sol. Phys., 121, 323
Rieger, E., Reppin, C., Kanbach, G., Forrest, D. J., Chupp, E. L., & Share, G. H. 1983, Proc. 18th Internat. Cosmic Ray Conf. (Bangalore), 10, 338
Ryan, J. M., & Lee, M. A. 1991, ApJ, 368, 316
Semukhin, P. E., & Kovaltsov, G. A. 1985, Proc. 19th Internat. Cosmic Ray Conf. (La Jolla) (NASA CP-2376), 4, 106
Smith, D. F., & Brecht, S. H. 1991, ApJ, 373, 289
Zweibel, E. G., & Haber, D. 1983, ApJ, 264, 648